


Article

Geometrical Optimization of Pump-As-Turbine (PAT) Impellers for Enhancing Energy Efficiency with 1-D Theory

Longyan Wang^{1,2,3,*}, Stephen Ntiri Asomani¹, Jianping Yuan^{1,2,*} and Desmond Appiah¹ 

¹ National Research Center of Pumps, Jiangsu University, Zhenjiang 212013, China; 5103170318@stmail.ujs.edu.cn (S.N.A.); bembo88donk@ujs.edu.cn (D.A.)

² Institute of Fluid Engineering Equipment, JITRI, Jiangsu University, Zhenjiang 212013, China

³ School of Chemistry, Physics and Mechanical Engineering, Queensland University of Technology, Brisbane 4001, Australia

* Correspondence: longyan.wang@connect.qut.edu.au (L.W.); yh@ujs.edu.cn (J.Y.)

Received: 24 June 2020; Accepted: 4 August 2020; Published: 10 August 2020



Abstract: This paper presents a multi-objective optimization strategy for pump-as-turbines (PAT), which relies on one-dimensional theory and analysis of geometrical parameters. In this strategy, a theoretical model, which considers all possible losses incurred (mainly by the components of pipe inlet, impeller and volute), has been put forward for performance prediction of centrifugal pumps operating as turbines (PAT). With the established mathematical relationship between the efficiency of PAT (both at pump and turbine mode) and the impeller controlling variables, the geometric optimization of the PAT impeller is performed with constant rotational speed. Specifically, the optimization data consist of 50 sets of impellers generated from Latin Hypercube Sampling method with its corresponding efficiencies calculated. Subsequently, the pareto-based genetic algorithm (PBGA) was adopted to optimize the geometric parameters of the impellers through the theoretical model. To validate the theoretical optimization results, the high-fidelity Computational Fluid Dynamics (CFD) simulation and the experimental data are employed for comparison of the PAT performance. The findings show that the efficiencies of both the pump and PAT optimized variables increased by 0.27% and 16.3% respectively under the design flow condition. Based on the one-dimensional theoretical optimization results, the geometry of the impeller is redesigned to suit both pump and PAT mode operations. It is concluded that the chosen design variables (b_2 , β_1 , β_2 , and z) have a significant impact on the PAT efficiency, which demonstrates that the optimization scheme proposed in this study is practicable.

Keywords: pump-as-turbine; theoretical model; energy performance prediction; 1-D theory calculation; optimization

1. Introduction

The global electricity production poses several problems that have been resolved over the years by different approaches to reduce its effect on the environment and operating costs. The generation of electricity using fossil fuels has significant implications for CO₂ pollution and depletion of the ozone layer. These pollution of CO₂ cause global warming, which is harmful to aquatic life and habitats as a whole [1]. The best solution for these environmental issues is definitely renewable energy which includes solar and wind power, biofuels and hydropower. However, the hydropower presents a desirable source of energy in all the renewable energy sources. Hydropower generates energy from water sources such as the ocean, rivers and waterfalls by hydraulic turbines. Hydraulic turbines are known for their high energy efficiency, but are relatively unattractive because of their high purchasing

costs for small hydropower [2]. Pump-as-turbine (PAT), as an alternative, is a conventional hydraulic pump that can be used in reversed mode to generate electricity in small hydropower plants. A PAT has many outstanding advantages when compared to hydraulic turbines. The PAT is a simple machine, easy to operate, with mass production, convenient maintenance and easily accessible [3,4]. The capital payback period of PAT has been estimated to be within two years in the range of 5–50 kW [5,6], which makes it a cost-effective alternative to hydraulic turbines. PAT is also applicable in many areas, such as the field of fertilizer production, water distribution network, water desalination, petro-chemical industry, and many other processes for energy production [7].

PAT provides technical solution for both economic suitability and system flexibility [8,9]. The introduction of PAT in the water-energy network has large potential in promoting energy savings practices [10]. A PAT can also be used for energy storage which function similarly to hydropower plants for pumped storage. According to Førsund [11], power can be produced by pumping water into a reservoir and then circulating it through a turbine components. The two-mode of operation in PAT or hydraulic power recovery turbine (HPRT) are applicable in the chemical process. First, the operation of the turbine decreases fluid pressure and at the same time permits the HPRT to retrieve part of the liquid energy and second, with a better design of the system, the pump mode operation will control the chemical process if the main pump is damaged [12].

As depicted in Figure 1, the flow direction shows the pump and PAT mode operations. The pump mode is a diffuse flow channel, which is due to the increase in flow area, thus from the tongue region to the exit area of the volute, while PAT mode is a contract flow channel, which is also due to the decrease in flow channel, thus from the throat area to the tongue of the volute. The contract flow channel hydraulic losses should be less than the diffuse flow channel, but the efficiency of the PAT is low when compared to the pump mode at off design flow conditions. Yang et al. [13] have reported that more than 50% of the total hydraulic losses in the PAT are attributed to the PAT impeller. As the pump is not suitable for operation in the PAT mode, its impeller are designed for forward rotation without taking the reverse mode operation into account.

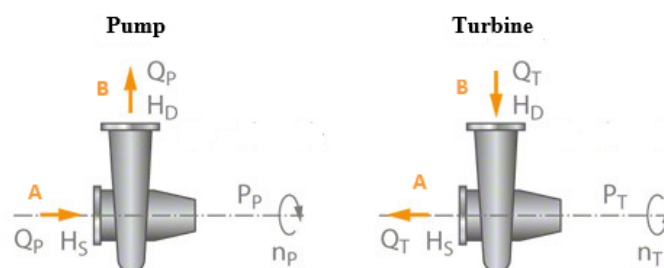


Figure 1. Flow direction of PAT operating in pump and turbine mode.

In addition to PAT issues, pump manufactures do not generally offer the performance curves of their pumps running in PAT mode, since this involves experimental testing of the pump in PAT mode, thus a considerable increase in the investment and testing costs [14]. The prediction of performance of a pump running in reverse mode is a current topic, which involves many research groups. In the recent years, different analyses have been carried out considering the losses inside the different components of this machine in reverse mode [15,16]. Some of these studies have proposed linkage for the prediction of PAT characteristics either by efficiency or specific speed of the pump, and some have also been experiments based on their relationships. Nevertheless, the results of these studies revealed an average deviation of $\pm 20\%$ from experimental data [17], with deviations in certain specific speed recoding more than 40% [18]. Many predictive techniques have been published until now, as reported by Ramos and Borga [19], Wang et al. [20], Derakhshan et al. [21], Li et al. [22], Sharma [23], Alatorre-Frenk [24], and Stepanoff [25]. In parallel with these studies, researchers like [23,26–29] proposed a theoretical model based on experimental data and concluded that PAT efficiency at the best efficiency point (BEP) in turbine mode is the same as in pump mode operating under the same working conditions.

Practically these formulas enable the user to determine the flow rate and the head used by the PAT at the BEP.

Since the pump is not perfectly designed to work in reverse mode, the optimization based on the PAT flow zone is required to improve the hydraulic machine performance. Furthermore, it should also be noted that the change of rotational speed of the pump under PAT mode can have significant influences on output performances of the machinery by comparison to the original pump mode since the best efficiency point of the pump and PAT mode may have a large discrepancy. However, there has been little research that focused on PAT optimization. Yang et al. [30] demonstrated that it would be more effective if the blade inlet angle value is within the range of 25–35° to ensure good performance. Derakhshan et al. [21,31] put forward a theoretical analysis to modify the geometry of the impeller and showed that it does directly affect the overall performance of the PAT. Furthermore, is highly expensive and time-consuming in pump design and optimization based on trial-and-error approach [32]. The combination of an optimization approach with CFD numerical simulation can, however, reduce the sequence of development and also reduce computational and experimental resources for performance enhancement.

For optimization procedures, theoretical 1-D calculations have proven to be extremely important tools for pump designers; they are useful in the measurement of geometric parameters in the very early stages in line with the requirements. Such measurements can easily decide whether the geometrical parameters selected are rational or not. Pump manufacturers, who desire to analyze their pump in details, in PAT mode, need tools that can enable them to predict the PAT mode geometric components and their influence on performance. Even though many researchers have worked on the energy prediction of PAT, very few researchers have worked on the theoretical optimization of PAT performance prediction. This study contributes to literature, by examining the geometrical parameters of the pump and PAT modes simultaneously to help explain the anomalous operation of PAT.

In this study, a theoretical attempt is made to optimize and predict the performance of centrifugal pump operating as PAT by modeling and analyzing all the various flow losses in the pump at each operating mode under constant rotational speed. The pareto-based genetic algorithm (PBGA) models were constructed to optimize the PAT and pump mode efficiencies. The design variables, i.e., the blade outlet width, blade exit angles, and the blade number, (b_2 , β_1 , β_2 , and z) were used as input parameters and the efficiencies of both pump and PAT at the design flow rate as the output parameters. In the following discussion, the theoretical model and flow losses of the pump and PAT are presented in detail. Afterwards, the PBGA algorithm was used to optimize the objective functions to identify the optimal parameters known as the pareto-frontiers solutions. In the end, the optimized values of the impeller is used to design new impeller that will suit both working conditions.

2. Theoretical Modeling of Pump and PAT

Here, 1-dimensional (1-D) theory is introduced for the description of the PAT working mechanism and further to formulate the realistic PAT working performance considering the head losses for the theoretical optimization study.

2.1. Ideal Pump and PAT Performance

The ideal theoretical head H_{th} , which is defined as the loss-free performance of a pump or turbine can be defined by means of Euler's equation and velocity triangles [26]. The pump and turbine velocity triangles as illustrated in Figure 2 are determined by the inlet and outlet geometry of the pump. The velocity triangle is made up of three velocities, namely absolute velocity, relative velocity and tangential velocity of the fluid and are denoted by v , w and u respectively. The absolute velocity of the fluid can be determined by the sum of the relative velocity and the tangential. For both operating mode, subscript 2 indicates the tip of the impeller and 1 the eye of the impeller. The flow angles α and β describe the relative and absolute velocity angles compared to the tangential velocity, respectively.

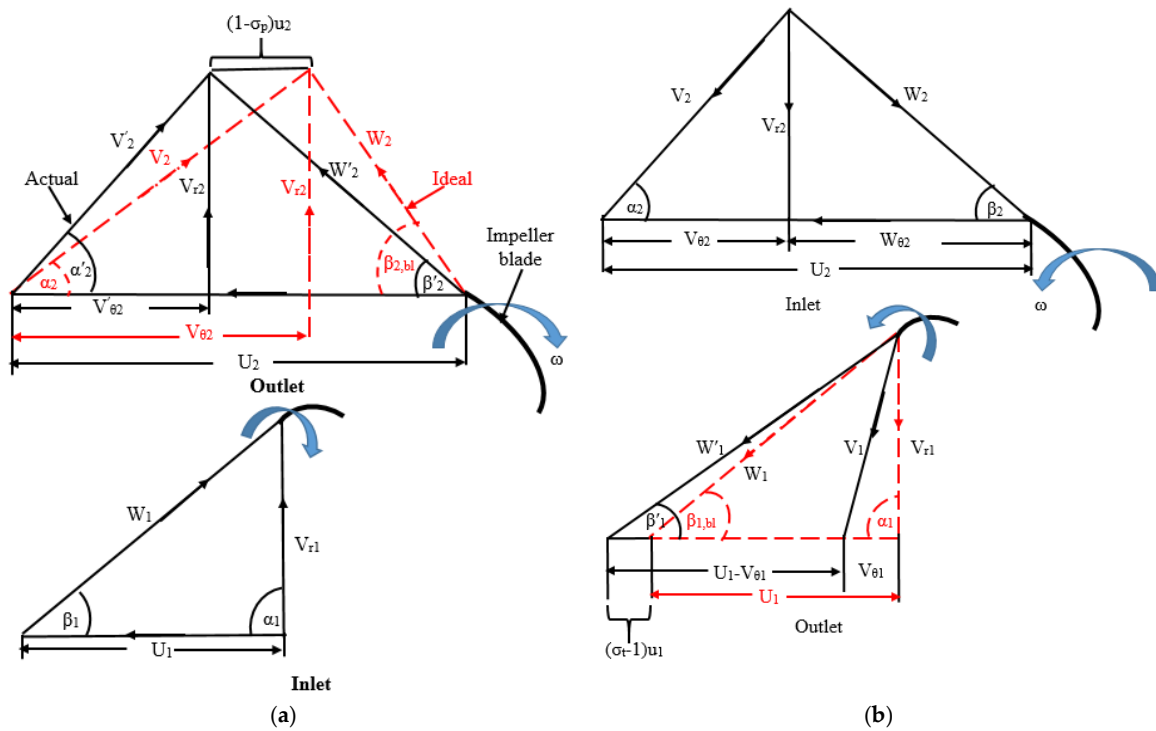


Figure 2. Inlet and outlet velocity triangles in (a) pump mode (b) turbine mode.

The theoretical head in both pump and turbine mode can be determined by Euler's equation for turbomachinery which is expressed as:

$$H_{th} = \frac{1}{g}(u_2 v_{\theta 2} - u_1 v_{\theta 1}) \quad (1)$$

where u (ms^{-1}) is the impeller (blades) longitudinal velocity, v_{θ} (ms^{-1}), is the tangential component of the absolute velocity, g (ms^{-2}), is the gravitational acceleration and H_{th} is the theoretical head (m).

In addition, the flow leaving the impeller of the machine is not correctly guided by the blades due to the slip phenomenon, which involves the reduction of the Euler's work. The slip factor in a pump and in a PAT is different due to opposite flows. The slip factor is defined as the ratio of actual and ideal values of the whirl velocity components at the outlet section of the impeller and it is expressed mathematically Equation (2) [33]:

$$\sigma = \frac{V'_{\theta}}{V_{\theta}} \quad (2)$$

By applying basic trigonometrical principles to Euler's equation for turbomachinery and velocity triangles, the theoretical head for both pump and turbine modes can be expressed as Equations (3) and (4) respectively:

$$H_{th,p} = \frac{u_{2,p}}{g} \left[u_{2,p} \sigma - \frac{Q \cot \beta_2}{A_{2,p}} \right] \quad (3)$$

$$H_{th,t} = \frac{1}{g} \left[u_{2,t} v_{r2,t} \cot \alpha_2 - u_{1,t}^2 \sigma + u_{1,t} v_{r1,t} \cot \beta_1 \right] \quad (4)$$

where v_r (ms^{-1}) is the radial velocity of the fluid, u (ms^{-1}) is the impeller longitudinal velocity, β° and α° are the flow angles and σ is the slip factor, where subscripts 1, 2, t and p depict the inlet, outlet, PAT mode and pump mode, respectively.

2.2. Pump and PAT Model

A centrifugal pump was employed as turbine in this study. The pump consists of six straight impeller blades and a spiral volute with a rectangular section. The pump design flowrate Q in pump mode is $25 \text{ m}^3/\text{h}$, and head is 8.5 m , with a rotating speed of 1450 r/min . The operational conditions of the pump mode is applied in the PAT mode. This pump operating as PAT is mainly composed of impeller with inlet and outlet diameter of 74 mm and 174 mm , respectively, and outlet width of 12 mm , with exit angles of 30° on the hub and shroud. The volute base diameter is 184 mm with inlet width of 20 mm . A summary of design parameters of the selected PAT model under study is listed in Table 1 and Figure 3 shows a sectional view of the pump impeller and volute in 2D while Figure 4 shows the actual pump structure.

Table 1. Geometrical and operational parameters of the studied Pump and PAT in pump mode.

Description	Parameter	Symbol	Unit	Value
Impeller	Outlet diameter	D_2	mm	174
	Inlet diameter	D_1	mm	74
	Outlet width	b_2	mm	12
	Blade number	z	-	6
	Hub diameter	D_h	mm	21
Volute	Inlet diameter	D_3	mm	184
	Inlet width	b_3	mm	20
	Tongue angle	θ	$^\circ$	27
	Nominal flow rate	Q	m^3/h	25
Operational Condition	Rotation speed	n	r/min	1450
	Efficiency	η	(%)	72.1
	Head	H	m	8.5

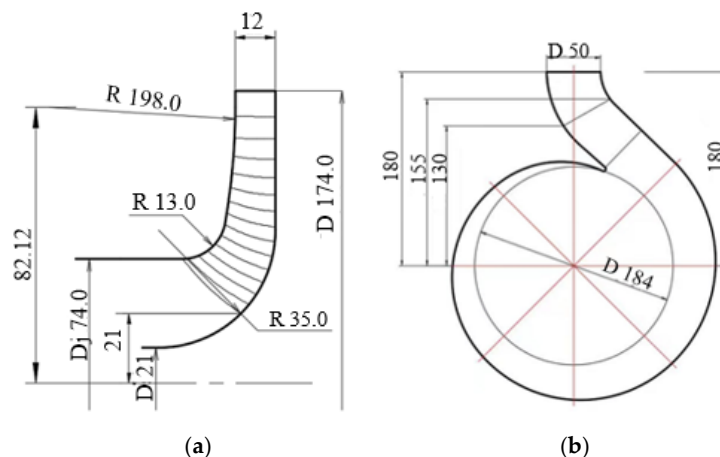


Figure 3. Sectional view of (a) Impeller (b) Volute.

2.3. Pump and PAT Head Losses

The geometrical parameters of the pump do not change when it works as turbine, only the flow and rotation direction changes. In addition, with the same rotational speed the mechanical losses, power losses due to leakage in turbine and pump modes are the same as stated by Derakshan et al. [34]. The PAT behavior is very complex and it is difficult to find a unique correlation for all pumps in reverse mode [34]. Furthermore, several expressions have to be solved to compute the hydraulic losses in the volute, impeller and outlet pipe. Therefore, since computing of hydraulic losses in PAT mode is somehow complex, these losses were estimated using pump mode.

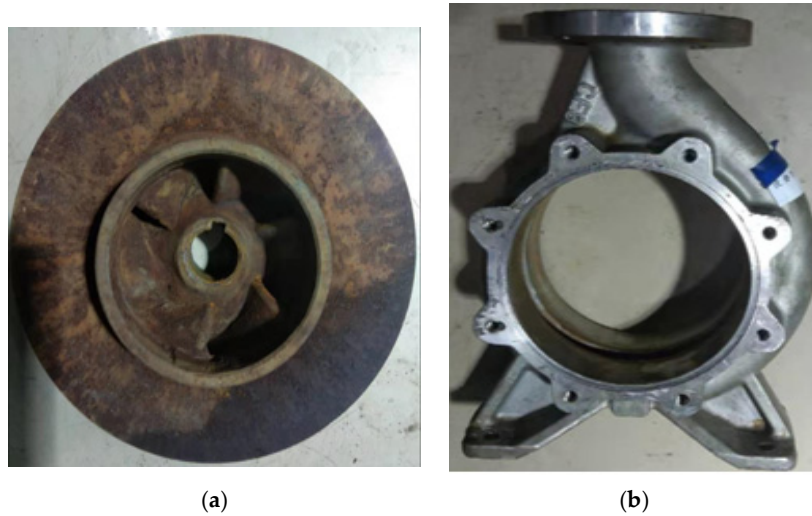


Figure 4. Pump model: (a) Impeller (b) Volute.

2.3.1. Pipe Inlet Losses

The inlet pipe in pump mode is used as the PAT outlet pipe and its hydraulic friction loss can be expressed as:

$$\Delta h_{\text{inlet}} = \lambda \frac{l_{\text{in}}}{D_{\text{in}}} \frac{v_0^2}{2g} \quad (5)$$

where l_{in} and D_{in} are the length and hydraulic diameter of the inlet pipe, λ denotes the friction coefficient depending on the Reynolds number, where v_0 denotes the axial velocity in the inlet pipe and is formulated as:

$$v_0 = \frac{Q}{\frac{\pi}{4}(D_j^2 - D_{jh}^2)} \quad (6)$$

where D_j denotes the inlet pipe diameter, D_{jh} denotes the impeller inlet hub diameter, Q denotes the flow rate. The friction coefficient λ is calculated on the basis of the Reynolds number and is defined as:

$$\lambda = \frac{0.3164}{\text{Re}^{1/4}} \quad (7)$$

2.3.2. Impeller Losses

Incidence Loss

The flow angle at the blade inlet is usually equal to the blade angle under design flow rate which can meet the design specifications of no incidence inlet. Generally, when the flow rate varies, the flow angle at the blade inlet is not equal to the blade angle. And this could result in flow separation on the blade surface resulting in loss of incidence. Under off-design flow condition the relative velocity w_1 decomposed into two relative velocity components w_{10} and Δw_1 as presented in Figure 5. Under designed flow rate the imaginary relative velocity w_{10} has the same direction of current from the no incidence inlet. The difference of the relative velocity Δw_1 is along the circumferential direction, representing the inlet incidence level. Thus, the incidence loss of blade inlet is defined as:

$$\Delta h_{\text{inc}} = f_{\text{inc}} \frac{\Delta w_1^2}{2g} \quad (8)$$

where f_{inc} denotes the coefficient of the incidence loss with a value between of 0.5–0.8, w (ms^{-1}) is the relative velocity of the flow, g (ms^{-2}) is the gravitational acceleration and Δh_{inc} is the incidence head loss (m) [35]. This effect is noticeable in both pump and PAT modes.

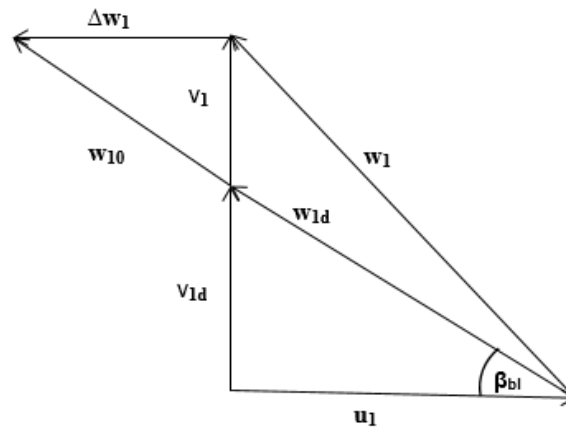


Figure 5. Velocity triangle under off-design condition (pump-mode) at impeller inlet.

The value of Δw_1 can be obtained by applying the triangle similarity theory with the velocity triangle in Figure 5, where the absolute velocity v_1 is proportional to the flow rate as expressed in Equation (9):

$$\Delta w_1 = u_1 \left(\frac{v_1 - v_{1d}}{v_{1d}} \right) = u_1 \left(\frac{Q - Q_d}{Q_d} \right) \quad (9)$$

where subscript d denotes under design flow rate, Q_d (m^3h^{-1}) is the design flow rate and v_{1d} (ms^{-1}) is the absolute flow velocity under design flow rate.

Sharma [23] put forward Equation (9) to predict the PAT mode design flow rate and head:

$$\frac{H_t}{H_p} = \frac{1}{\eta_t^{1.2}}, \quad \frac{Q_t}{Q_p} = \frac{1}{\eta_p^{0.8}}, \quad \eta_p = \eta_t, \quad P_p = P_t \quad (10)$$

where H_t (m) is the pressure head in turbine mode, H_p (m) is the pressure head in pump mode, η_t is the efficiency of the turbine mode, η_p is the efficiency of the pump mode, Q_t (m^3h^{-1}) is the design flow rate of the turbine mode, Q_p (m^3h^{-1}) is the design flow rate of the pump mode, P_p (W) is the power of the pump mode and P_t (W) is the power of the turbine mode.

Surface Frictional Loss

In both pump and PAT modes the friction is known as a linear loss due to the fluid viscosity effects of the wall boundary layer of the blade, impelling chamber etc. The impeller hydraulic friction head loss Δh_{sfl} is calculated by the flow theory via pipes and is given by [36]:

$$\Delta h_{sfl} = 4C_d \frac{L_b}{D_{hyd}} \frac{W^2}{2g} \quad (11)$$

where D (mm) is the impeller diameter, w (ms^{-1}) is the relative velocity of the fluid, β° is the blade angle, Δh_{sfl} is the surface frictional head loss in meter (m), C denotes the corresponding wetted perimeter, S denotes the impeller passage sectional area and D_{hyd} denotes the hydraulic diameter of impeller passage. Subscript 1 and 2 denote inlet and outlet of the impeller.

The hydraulic diameter and the average relative velocity are given, respectively, as, Gülich [36]

$$D_{hyd} = \frac{2(d_j b_1 + d_2 b_2)}{d_j + b_1 + d_2 + b_2} \quad (12)$$

$$W = \frac{Q_i / z}{(d_j b_1 + d_2 b_2) / 2} \quad (13)$$

The blade length is given as:

$$L_b = \frac{1}{2} \left(\frac{d_2 - d_j}{d_2} \right) \frac{1}{\sin\left(\frac{\beta_{bl1} + \beta_{bl2}}{2}\right)} \quad (14)$$

The impeller dissipation coefficient is given as, Gülich [36]

$$4C_d = (f_i + 0.006) \left(1.1 + 4 \frac{b_2}{d_2} \right) \quad (15)$$

The impeller friction coefficient f_i is function of the average impeller Reynolds number Re and the roughness κ [37]:

$$f_i = \frac{0.3086}{\left(\log \left[(6.9/Re) + \left((k/D_{hyd})/3.7 \right)^{1.11} \right] \right)^2} \quad (16)$$

where κ denotes roughness factor as:

$$\frac{k}{D_{hyd}} = \frac{(k/d_2)}{(D_{hyd}/d_2)} \quad (17)$$

Blade Loading Loss

The blades loading loss originates from the pressure differential between the pressure and the suction side of the impeller, which affects the separation of the secondary flow and the boundary layer within the pump and PAT modes. Lieblein, Schwenk [38], Coppage and Dallenbach [39] have developed the calculation equation of the diffuser factor and the calculation equation of the blade loading loss as:

$$\Delta h_{bl} = \frac{0.05 D_f^2 u_2^2}{g} \quad (18)$$

where u_2 is the average circumferential velocity at impeller outlet, g (ms^{-2}) is the gravitational acceleration, Δh_{bl} is the blade loading head loss (m) and D_f is the diffuser factor and is formulated as:

$$D_f = 1 - \frac{w_2}{w_{1t}} + \frac{0.75 g H_{th}}{u_2^2} \frac{1}{\frac{z}{\pi} \left(1 - \frac{D_{jt}}{D_2} \right) + \frac{2 D_{jt}}{D_2}} \frac{w_2}{w_{1t}} \quad (19)$$

where w_{1t} (ms^{-1}) is the relative velocity at tip of impeller inlet, w (ms^{-1}) is the relativity velocity of the impeller outlet, H_{th} (m) is a theoretical head, D_{jt} (mm) is the diameter at the tip of the inlet, D_2 (mm) is the average diameter of the outlet, z , is the blade number and u (ms^{-1}) is the impeller (blades) longitudinal velocity.

The flow in the rotor is increased with a positive pressure gradient in PAT mode and therefore separation, wake mixing, and recirculation can therefore be ignored in PAT mode because its influence on the hydraulic performance is insignificant. Therefore the separation, wake mixing and recirculation flow losses discussed are for the pump mode operation.

Separation Loss

The separation may occur in the impeller at any point. According to Tuzson [40], if the ratio of the relative velocity at the inlet w_1 and the outlet w_2 exceeds a value of 1.4, a portion of the velocity head difference is lost, and is expressed as:

$$\Delta h_{sl} = 0.25 \left[\left(\frac{w_1}{w_2} \right)^2 - 2 \right] \frac{w_2^2}{2g} \quad (20)$$

where w_1 and w_2 are the relative velocity of the inlet and outlet respectively, Δh_{sl} (m), is the separation head loss and g (ms^{-1}) is the gravitational acceleration. Subscript 1 and 2 denote the inlet and outlet of the impeller.

Recirculation Loss

Impellers with relatively large inlet diameters are mostly likely to recirculate and are usually found in high specific pumps. The appearance of inlet recirculation results in parasitic power demand. The recirculation power loss can be formulated as, [41]:

$$\Delta P_{\text{rec}} = 0.03 \rho g Q^* \frac{(\tan(\frac{\pi}{2} - \alpha_2)) D_f^2 u_2^2}{g} \quad (21)$$

$$Q^* = Q + \Delta Q_{lk} \quad (22)$$

where Q^* (m^3/h) is the ideal flow rate; D (mm) is the diameter of the impeller; α_2 denotes the impeller outlet absolute flow angle under pump mode; ΔQ_{lk} is the leakage flow rate; ΔP_{rec} (W) is the recirculation power loss.

Wake Mixing Loss

The jet/wake phenomenon occurs at the impeller outlet, which results in wake mixing loss. This phenomenon takes place due to the divergent shape and abrupt expansion on the trailing edge of the impeller. The wake mixing loss is formulated by [42] as:

$$\Delta h_{\text{mix}} = \left[1 - \frac{(1 - \varepsilon_{\text{wake}}) b_2}{b_3} \right]^2 \left(\frac{1}{1 - \varepsilon_{\text{wake}}} \right)^2 \frac{v_2}{2g} \quad (23)$$

where b_2 denotes the impeller outlet blade width, b_3 denotes the volute width, Δh_{mix} (m) is the wake mixing head loss and $\varepsilon_{\text{wake}}$, denotes the wake coefficient, which is formulated as:

$$\varepsilon_{\text{wake}} = 1 - \frac{w_2}{w_1 / 1.4} \quad (24)$$

Disk Friction Loss

When calculating the shaft power demand, the disk friction power is divided by the flow rate and the pressure head, which is added to the theoretical head. [43] formulated the disk friction loss as expressed in Equation (19), which is applicable in both pump and PAT operations.

$$\Delta P_{df} = f_{df} \rho D_2^2 u_2^3 \quad (25)$$

where f_{df} , denotes the coefficient of the disk friction loss which can be formulated as:

$$f_{df} = \frac{0.166875}{\text{Re}_{df}^{0.5}}, \quad \text{Re}_{df} < 3 \times 10^5 \text{ or } \frac{0.0038875}{\text{Re}_{df}^{0.2}}, \quad \text{Re}_{df} > 3 \times 10^5 \quad (26)$$

and Re_{df} is the Reynolds number, which can be calculated as:

$$\text{Re}_{df} = \frac{\rho u_2 D_2}{2\mu} \quad (27)$$

where f_{df} , is the loss coefficient of the disk friction, ΔP_{df} (W) is the disk friction power loss and μ is the dynamic viscosity of the medium.

Leakage Loss

In both pump and PAT mode operations, the leakage flow, which is induced by the gap between impeller and casing is defined by [40] as:

$$\Delta P_{lk} = \rho g \Delta Q_{lk} H_{th} \quad (28)$$

$$\Delta Q_{lk} = C_{lkf} A_{lk} \sqrt{2g\Delta H_m} \quad (29)$$

$$C_{lkf} = \frac{1}{\sqrt{1 + 0.5\eta_{lk} + \frac{\lambda_{lk} \times X_{lk}}{2Y_{lk}}}} \quad (30)$$

$$A_{lk} = D_j \pi Y_{lk} \quad (31)$$

$$\Delta H_m = \frac{3}{4} \frac{u_2^2 - u_1^2}{2g} \quad (32)$$

where C_{lkf} denotes the leakage flow rate coefficient, X_{lk} and Y_{lk} denote the axial and radial distance of ring clearance respectively, λ_{lk} is hydraulic resistance coefficient within clea flow in the range of 0.04–0.06, η_{lk} denotes the rounded coefficient at the inlet of ring clearance in the range of 0.5–0.9.

2.3.3. Volute Losses

The volute component direct the flow from the impeller exit and leads it into the discharge area, converting the kinetic energy into pressure energy in pump mode and vice-versa in PAT mode [44]. The flow enters the volute with a through velocity v_3 , which is decomposed into a velocity parallel to the direction of the volute v_{3p} , and tangential to the direction of the impeller v_{3d} . The flow then exits the volute with a velocity $v_4 = Q/A_{th}$ [45], which is given as:

$$v_4 = \frac{\eta_v \varepsilon_2 A_2 v_{r2}}{\tan \alpha_v \pi d_3 b_3} \quad (33)$$

where:

$$\tan \alpha_v = \frac{A_{vth}}{A_2 (d_3/d_2)(b_3/b_2)} \quad (34)$$

$$v_3 = \frac{v_4}{\cos \alpha_v} \quad (35)$$

$$v_{3d} = v_{\theta 2} - v_4 \quad (36)$$

where η_v is the volumetric efficiency, ε is blade thickness coefficient, d_2 (mm) is the diameter of the impeller outlet, d_3 (mm) is the base circle diameter of the volute, b_3 (mm) is the volute inlet width, b_2 (mm) is the blade outlet width, α_v is the volute angle, v_3 (ms^{-1}) is the volute inlet velocity, v_4 (ms^{-1}) is the volute outlet velocity, v_{3d} (ms^{-1}) is the circulation velocity of the flow in the volute, v_{3p} (ms^{-1}) is the volute flow velocity and v_{θ} (ms^{-1}) is the tangential absolute velocity of the flow in the impeller and A_{vth} is the volute throat inlet area.

Incidence Loss of Spiral Part

The incidence loss of the spiral part inlet can be determined by:

$$\Delta h_{lv} = k_{lv} \frac{(v_{\theta 2} - v_{th})^2 + v_{r2}^2}{2g} \quad (37)$$

where k_{lv} denotes the coefficient of the incident mix loss, which is 0.45 [46], v_{th} (ms^{-1}) is the velocity of the flow inside the sections that connect the volute spiral part and diffuser part together, v_r (ms^{-1}) is the

radial velocity in the impeller, g (ms^{-2}) is the gravitational acceleration and v_θ (ms^{-1}) is the tangential absolute velocity of the flow in the impeller.

Friction Loss of Spiral Part

Volute friction loss is determined by using the theory of flow through pipes, which can be formulated in both pump and PAT modes as [47]:

$$\Delta h_{vfl} = 4f \frac{d_3 b_3 v_4^2}{d_h^2 2g} \quad (38)$$

where d_3 (mm) is the base circle diameter of the volute, b_3 (mm) is the volute inlet width, v_4 (ms^{-1}) is the volute outlet flow velocity, g (ms^{-2}) is the gravitational acceleration, d_h is the average volute hydraulic diameter, and f is the volute friction loss coefficient, which is a function of both volute roughness ε and Reynolds number Re :

$$d_h = \frac{d_2}{\frac{1}{2(b_3/b_2)(b_2/d_2)} + \frac{1}{8(\pi/z)(d_3/d_2)(\sin \alpha_v)}} \quad (39)$$

$$f = 0.25 \left(\log \left(\frac{\varepsilon}{d_h} + \frac{5.74}{Re^{0.9}} \right) \right)^{-2} \quad (40)$$

$$Re = \frac{\bar{w} d_h}{\nu} \quad (41)$$

where \bar{w} (ms^{-1}) is the arithmetic average between the relative velocities and ν (m^2s^{-1}) is the kinetic viscosity of the fluid, α_v is the volute angle and z is the blade number.

Friction Loss of Diffuser Part

The diffuser component divergent structure can lead to separation of the boundary layer and can cause losses in pump mode. In PAT mode diffuser, part of the volute serves as a contraction flow passage and is expressed mathematically as:

$$\Delta h_{vdiff} = k_{vdiff} \sin \theta \left(\frac{A_5}{A_4} - 1 \right)^2 \frac{A_5^2}{2g} \quad (42)$$

$$\theta = 2 \arctan \left(\frac{\sqrt{A_5/\pi} - \sqrt{A_4/\pi}}{l_{diff}} \right) \quad (43)$$

where k_{vdiff} denotes the diffuser loss coefficient, which is 6.5 [46], A_5 (m^2) denotes the diffuser outlet area, A_4 (m^2) denotes the volute inlet (volute throat) area, l_{diff} denotes the diffuser passage length and v_4 denotes the velocity at the outlet and θ° correspond to the diffuser angle.

As already mentioned, under PAT mode operation, the diffuser part of the volute will serve as a contraction part and in pump mode acts as diffusion part, thus, the separation loss can be neglected in PAT mode and be considered in pump mode operation only.

Separation Loss of Diffuser Part

$$\Delta h_{vsf} = f_v \frac{1}{8 \tan(\theta/2)} \left[\left(\frac{A_5}{A_4} \right)^2 - 1 \right] \frac{v_4^2}{2g} \quad (44)$$

where f_v denotes the volute friction loss coefficient and θ° corresponds to the diffuser angle.

2.4. Realistic PAT Performance

The losses in the inlet and outlet pipe, impeller, and volute have been modeled, and the total hydraulic loss and efficiency for both pump and PAT can be determined by adding up all the losses above. The total head loss, the actual pump head and pump efficiency have been expressed in Equations (45)–(47):

$$\Delta h_{TOT} = \Delta h_{inlet} + \Delta h_{inc} + \Delta h_{sfl} + \Delta h_{bl} + \Delta h_{sl} + \Delta h_{mix} + \Delta h_{vl} + \Delta h_{vfl} + \Delta h_{vdiff} + \Delta h_{vsl} \quad (45)$$

The actual head H_p under pump mode can be expressed as:

$$H_p = H_{th,p} - \Delta h_{TOT} \quad (46)$$

where H_p (m) denotes the actual head loss under pump mode, Δh_{TOT} (m) denotes the total head loss and $H_{th,p}$ (m) denotes the theoretical head loss in pump mode.

Additional losses, which includes the disk friction power loss, leakage loss and the recirculation power loss, are added into the expression to calculate the total efficiency of the pump as expressed in Equation (47) as:

$$\eta_p = \frac{\rho g Q H_p}{\rho g Q H_{th,p} + \Delta P_{rec} + \Delta P_{df} + \Delta P_{lk}} \quad (47)$$

where ρ (kgm^{-3}) is the density of the fluid, g (ms^{-2}) is the gravitational acceleration, Q (m^3h^{-1}) is the flow rate, H_p (m) is the actual head loss under pump mode, ΔP_{df} (W) is the disk friction power loss, ΔP_{lk} (W) is the leakage power loss, ΔP_{rec} (W) is the recirculation power loss and $H_{th,p}$ (m) is the theoretical head in pump mode.

According to the above study, the theoretical model for the PAT mode performance is established in Equations (48)–(50):

$$\Delta h_{TOT} = \Delta h_{vdiff} + \Delta h_{vfl} + \Delta h_{inc} + \Delta h_{sfl} + \Delta h_{bl} + \Delta h_{outlet} \quad (48)$$

$$H_T = H_{th,t} + \Delta h_{TOT} \quad (49)$$

where H_T (m) denotes the actual head loss under PAT mode, Δh_{TOT} (m) denotes the total head loss and $H_{th,t}$ (m) denotes the theoretical head loss under PAT mode.

The expression for calculating the total PAT efficiency, η_t , is presented as:

$$\eta_t = \frac{\rho g H_{th}(Q - \Delta Q) - \Delta P_{df} - \Delta P_{lk}}{\rho g Q H_T} \quad (50)$$

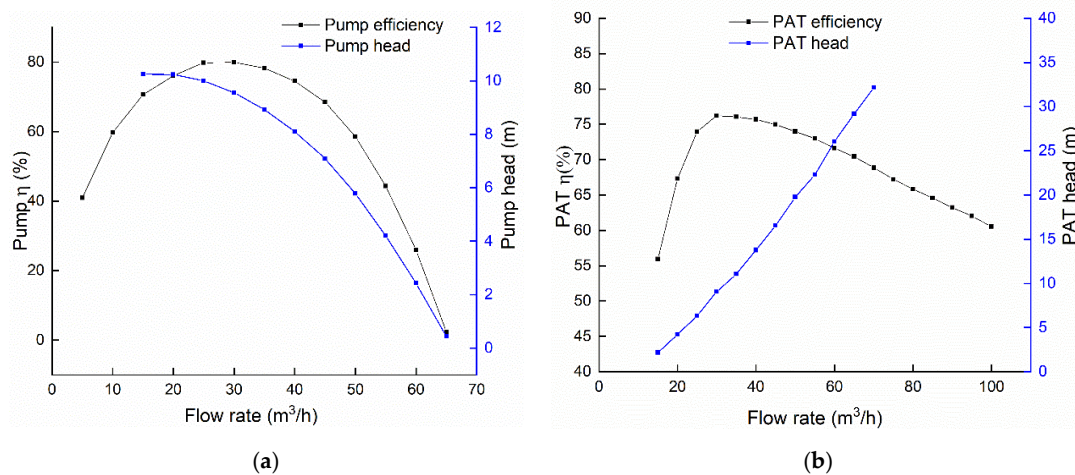
where ρ (kgm^{-3}) is the density of the fluid, g (ms^{-2}) is the gravitational acceleration, Q (m^3h^{-1}) is the flow rate, H_T (m) is the actual head loss under PAT mode, ΔP_{df} (W) is the disk friction power loss, ΔP_{lk} (W) is the leakage power loss and $H_{th,t}$ (m) is the theoretical head in PAT mode.

Table 2 lists the necessary input parameters that are needed for the theoretical model. The appropriate velocity may be calculated from the hydraulic equations according to the parameters specified, and then the hydraulic losses can be determined.

Figure 6 displays the theoretical model's performance curves for the pump and turbine modes. Under turbine mode the BEP switches to a higher flow rate than the pump mode. Under turbine mode, the maximum efficiency of 75.48% was below 79.82% under pump mode. The pump and turbine heads are 9.60 m and 9.14 m respectively under the best efficiency point. The turbine performance characteristic curve is almost flat in comparison with pump mode under high flow rates. This high efficiency region under turbine mode is essential for the safe and stable operation. Both the pressure head of the pump and turbine modes decrease and increase respectively with the increase in flow rate, and also show a linear correlation with the flow rate.

Table 2. Theoretical model input parameters.

Type	Parameter	Unit	Definition
Physical constant	g	9.8 m/s^2	Acceleration due to gravity
Physical parameters	ρ	997 kg/m^3	Density
Design parameter	Q_p	$25 \text{ m}^3/\text{h}$	Pump mode flow rate
	n	1450 rpm	Rotational speed
Geometrical parameters	D_{1h}	21 mm	Diameter of the impeller inlet Hub
	D_j	74 mm	Diameter of the impeller inlet Shroud
	D_2	174 mm	Impeller outlet diameter
	b_2	12 mm	Impeller outlet blade width
	β_{1h}	43°	Blade angle at impeller inlet Hub
	β_{1s}	12°	Blade angle at impeller inlet Shroud
	β_{2h}	30°	Blade angle at impeller outlet Hub
	β_{2s}	30°	Blade angle at impeller outlet Shroud
	z	6	Impeller Blade number
	D_0	84 mm	Suction pipe diameter
	l_{suc}	200 mm	Suction pipe length
	D_3	184 mm	Volute base circle diameter
	A_4	1279.2 mm^2	Volute area of 8th section
	φ	27°	Volute tongue angle
	b_3	20 mm	Volute width
Model coefficient	f_{inc}	0.7	Incidence loss coefficient
	f_{seq}	0.61	Flow separation loss coefficient
	k_{vmix}	0.45	Incidence mix loss coefficient
	k_{vdiff}	6.5	Diffuser loss coefficient

**Figure 6.** Performance curve of pump and PAT: (a) pump mode (b) PAT mode.

3. Optimization Procedure

The procedure for optimization is shown in Figure 7. This comprises of 4 steps in all: the design of method (DoE) of Latin hypercube sampling (LHS), 1-D calculation procedure, Pareto-Based Genetic Algorithm, and result verification by CFD.

The initial process is to sample the input variables based on design of experiment method. The input variables were chosen according to the respective design targets and the importance level of the design variables on the targets themselves. Secondly, a series of impellers were modelled theoretically by considering all flow losses inside the hydraulic machinery (PAT) with Matlab programming code (R2016a, MathWorks, USA). This model allows user to predict the efficiencies of the pump and turbine mode simultaneously under design flow condition by means of varying the design variables.

The efficiencies obtained from the pump and PAT modes were selected as objective functions. The fourth part was to solve the models using the Pareto-Based Genetic algorithm to obtain 2D Pareto solutions. Finally, the optimized cases were verified by a computational fluid dynamic CFD model to improve the reliability of the results.

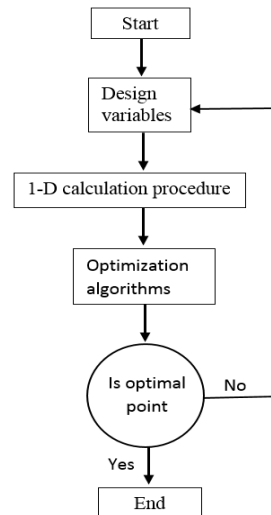


Figure 7. Flowchart of the optimization process.

3.1. Objective Functions

The objective of this study is to simultaneously maximize the efficiency of pump and PAT modes (η_p and η_t , respectively) at the design flow rate. The objective functions are defined as follows:

$$\eta_p = \frac{\rho g Q H_p}{\rho g Q H_{th,p} + \Delta P_{rec} + \Delta P_{df} + \Delta P_{lk}} \quad (51)$$

$$\eta_t = \frac{\rho g Q H_T - \Delta P_{df} - \Delta P_{lk}}{\rho g Q H_{th,t}} \quad (52)$$

where g , ρ , Q , H , P and Δh are representing the acceleration caused by gravity, fluid density, flow rate, pressure head, power and change in hydraulic head loss, respectively. Subscript p , t , th , rec , df , lk are pump mode, turbine mode, theoretical, recirculation loss, disk frictional loss and leakage loss respectively.

3.2. Decision Variables

In order to achieve the optimization, realistic design points must be specified within the range of design variables. Four design points were therefore selected with the Latin hypercube sampling method (LHS) [48]. According to the study concerning the effect of various parameters on the performance of PAT, the geometric parameters including blade outlet width b_2 , blade inlet and exit angles β_1 and β_2 on the hub and shroud, and the blade number z were selected as the input design variables. Table 3 presents a summary of the design variables.

Table 3. Range of design variables.

Boundary	b_2	β_2	β_1	z
Lower	0.010	20	20	4
Upper	0.015	35	35	8

The Latin Hypercube Sampling Method [49], which is a very useful experiment design method was applied to establish a discrete points in the design space, 50 cases of the impeller were created randomly due to the requirement of sufficient data for the construction of nonlinear operation. Some of the designed variables combination are listed in Table 4, which shows the target values at the design point in the optimization process calculated by the theoretical model.

Table 4. Some of the 50 impellers and calculated efficiencies.

No.	b_2	β_2	β_1	z	PAT η (%)	Pump η (%)
1	0.011	27.48	26.66	6	70.28	90.07
2	0.012	25.83	24.47	6	76.69	90.76
3	0.012	20.38	20.85	5	82.30	91.12
4	0.014	25.30	29.79	6	73.09	90.02
5	0.014	23.45	27.85	8	71.10	90.82
6	0.012	22.63	30.33	4	62.81	89.12
7	0.012	32.02	27.02	6	79.94	89.52
...
46	0.015	26.16	31.12	4	68.51	91.22
47	0.014	20.14	27.63	6	66.68	90.11
48	0.014	25.63	34.10	6	76.44	89.15
49	0.015	31.67	32.66	7	75.59	89.77
50	0.013	22.38	26.12	5	80.26	88.83

3.3. Orthogonal Test

The orthogonal array design of four factors signifying the number of design variables and twelve runs L12 is established in Table 5. This test is very significant because it reveals the level of influence each design variables that have on the objective function.

Table 5. Orthogonal array design.

1	1	1	1
1	1	1	1
1	1	2	2
1	2	1	2
1	2	2	1
1	2	2	2
2	1	2	2
2	1	2	1
2	1	1	2
2	2	2	1
2	2	1	2
2	2	1	1

Investigations were performed at the design flow rate according to the objective functions of the optimization. The results from the orthogonal test are offered in Table 6. From a direct analysis, it was observed that the majority of the combinations can satisfy the individual objectives, however, deciding the best scheme from the orthogonal results became problematic. It is, therefore, necessary to conduct a range analysis to understand the extent to which each design variable affects the optimization target.

To determine the variance, R , the difference between the maximum and minimum values was analyzed for each factor at all levels. The mathematical relation for the range analysis [50,51] is expressed as:

$$R = \max(k_1, k_2, \dots, k_i) - \min(k_1, k_2, \dots, k_i) \quad (53)$$

$$k_i = \frac{1}{N_i} \sum_{j=1}^{N_i} y_{ij} \quad (54)$$

$$K_i = \sum_{i=1}^{N_i} y_{ij} \quad (55)$$

where, K_i is the sum of the values of the levels for each factor, k_i is the average value, y_{ij} is performance value for the factor, and i and j are the number of levels and number of factors, respectively.

Table 6. Orthogonal test.

b_2	β_2	β_1	z	Pump η (%)	PAT η (%)
0.010	20	20	4	92.84	81.06
0.010	20	20	4	92.84	81.06
0.010	20	35	8	86.16	0
0.010	35	20	8	81.86	63.81
0.010	35	35	4	88.64	73.28
0.010	35	35	8	81.86	42.43
0.015	20	35	8	91.46	48.77
0.015	20	35	4	86.48	48.44
0.015	20	20	8	91.46	81.22
0.015	35	35	4	84.87	87.49
0.015	35	20	8	88.62	82.75
0.015	35	20	4	84.87	94.08

It can be seen from Table 7 and Figure 8 that the order of influence of the parameters is $\beta_1 > z > \beta_2 > b_2$. This means that for a single objective of maximizing only PAT efficiency, β_1 has a primary influence on the target. The trend was however different for the objective of the pump efficiency. It is seen from Table 8 and Figure 9 that the order of influence of the parameters is $\beta_2 > b_2 > \beta_1 > z$.

Table 7. Range analysis of PAT efficiency.

Level	b_2	β_2	β_1	z
1	52.12	51.9	80.58	76.87
2	73.79	73.97	50.07	53.16
Delta	21.68	22.08	30.52	23.71
Rank	4	3	1	2

Table 8. Range analysis of pump efficiency.

Level	b_2	β_2	β_1	z
1	86.27	89.68	87.93	87.54
2	87.96	85.12	86.58	86.90
Delta	1.69	4.56	1.35	0.64
Rank	2	1	3	4

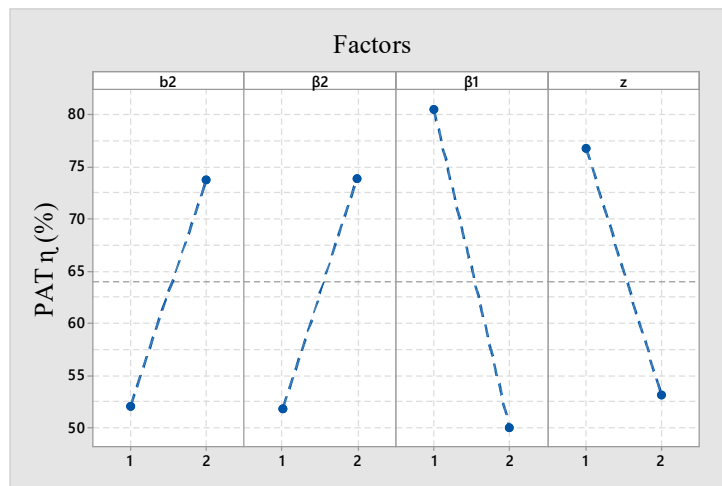


Figure 8. Level of influence of each parameter on PAT efficiency.

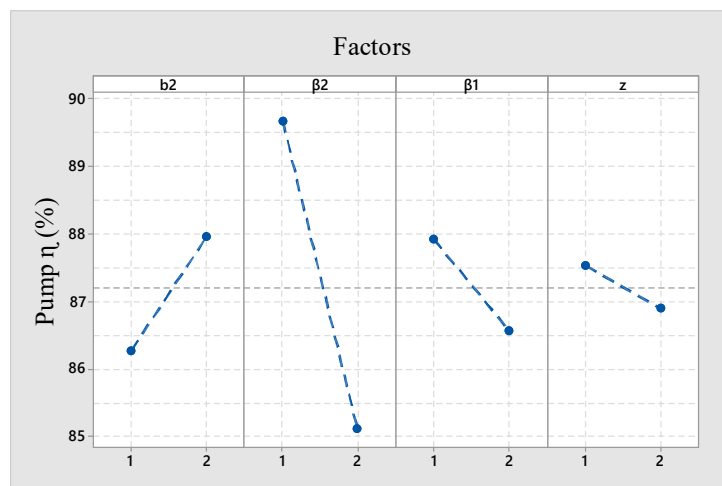


Figure 9. Level of influence of each parameter on pump efficiency.

This implies that for a single objective of maximizing the pump efficiency, β_2 has a high influence on the target space. The two parameter combinations are both not the optimum parameters since it is obvious that any attempt to improve one parameter makes at least one of the parameters worse off. The problem is therefore a multi-objective problem and would require a multi-objective approach to obtain a parameter combination that would increase both the efficiency of pump and PAT simultaneously.

3.4. Multi-Objective Optimization Design

A multi-objective optimization is applied to maximize or minimize objective functions when there are two or more objective functions under the same variable constraints. A Pareto-optimal approach, also called the Pareto frontiers, is applied to elucidate problems of this nature, since it is basically not possible to obtain a solution that would optimized all objective functions. This is because one parameter usually gets worse when any other parameter is enhanced. Under such conditions, the Pareto frontier, which is an efficiency solution, is used to control optimal combinations of parameters which would better solve the problem. The Pareto-based genetic algorithm (PBGA) was applied [52] in the study to obtain the global Pareto frontier of the two objective functions expressed in Equation (56). The Matlab function codes gamultiobj [53] was applied for the implementation of the multiobject algorithm.

This approach has the potential to use a controlled elitist, which gives it an advantage over the simple genetic algorithm and has been successfully employed in other optimization works [54–56].

$$\text{find} \left\{ \begin{array}{ll} \max & \eta_p = f_1(b_2, \beta_2, \beta_1, z) \\ \max & \eta_t = f_2(b_2, \beta_2, \beta_1, z) \\ \text{s.t.} & \\ & 0.010 \leq b_2 \leq 0.015 \\ & 20 \leq \beta_2 \leq 35 \\ & 20 \leq \beta_1 \leq 35 \\ & 4 \leq z \leq 8 \end{array} \right. \quad (56)$$

Since the objective functions are more than one, it is not possible to use the value of each function to determine the individual efficiencies. The expression in Equation (57) was introduced to determine the individual efficiency and solve the problem:

$$F(x) = \left[\frac{1}{1 + \|x - y\|_2} \right] \quad (57)$$

where, x : indicates any single population individual; y : indicates the Pareto efficient individual closet to x and $\|x - y\|$ indicates the Euclidean distance between x and y . In the construction of the Pareto-optimal solutions the following input parameters were applied. This means population size of 100, Pareto-front population of 0.8, crossover fraction of 0.85, 1000 generations, and function tolerance of 10.

4. Results and Discussions

4.1. Validation of the Theoretical Results

4.1.1. CFD Simulation of PAT Model

Numerical investigation was considered as a first method of validation of the proposed theoretical model in absence of experimental measurements. The numerical methods and boundary condition settings were chosen based on the steps outlined by Yang et al. [13]. Figure 10 shows the computational flow domain of the PAT model. It depicts the six blades impeller, inlet and outlet pipe with radial volute.

The numerical methods and boundary condition settings were chosen based on the steps outlined in the reference [57]. Hexahedron structured mesh was generated for all the domains, the meshed impeller blades and the volute have been depicted in Figure 11. Before for optimization process the mesh quality, mesh number and numerical simulations are crucial. A structured grid for the computational domain was used to build by using ANSYS-ICEM. The grids are defined in the near-wall flow regions and the grid numbers was used to check the mesh independence performed. When the grid number is about 2.9 million, the variation of head was within 0.2% as indicated in Figure 12. Therefore, the total number of grids was set to be 2.9 million to save computing time.

In both pump and PAT modes the steady state numerical calculations are set as follows. The Reynolds-averaged Navier–Stokes (RANS) equations are solved using CFX software (19.0, ANSYS, USA) at different operating conditions. The steady state simulations were performed with interface model set to frozen rotor. The fluid material was water at 25 °C. The boundary condition of the suction pipe inlet was defined as static pressure of 1atm while the discharge pipe outlet was defined as mass flow. For the steady state simulations, a convergence criterion of 1.0×10^{-6} was selected. In order to predict the highly turbulent flow patterns within the pump, the SST $k-\omega$ is implemented for the numerical simulations with a 5% turbulent intensity. The wall roughness of every boundary of each domain was set as “smooth wall”, while the mass and momentum setting was set to “no slip wall”.

The impeller was set to operate at 1450 r/min for the PAT mode. Though we fix the rotational speed of the impeller for facilitating the research, it should also be noted that the change of rotational speed of the pump under PAT mode can have significant influences on output performances of the machinery when compared to the original pump mode since the best efficiency point of the pump and PAT mode may have a large discrepancy. By changing flow conditions, both pump and PAT modes characteristic curves were obtained.

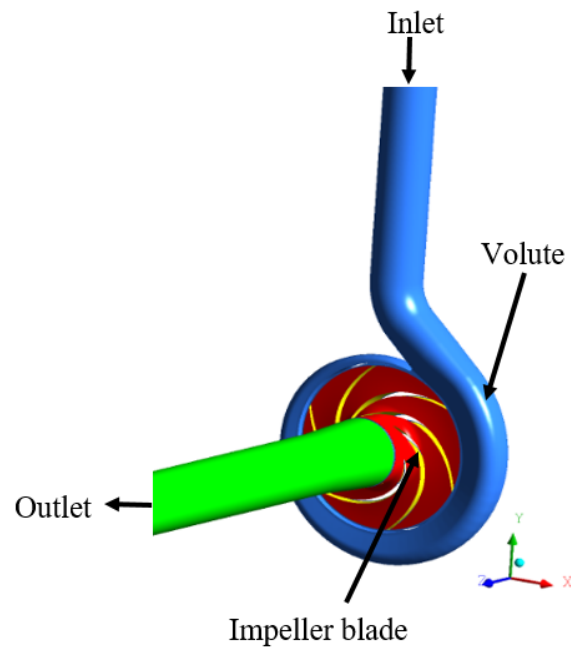


Figure 10. Flow domain of the baseline PAT model.

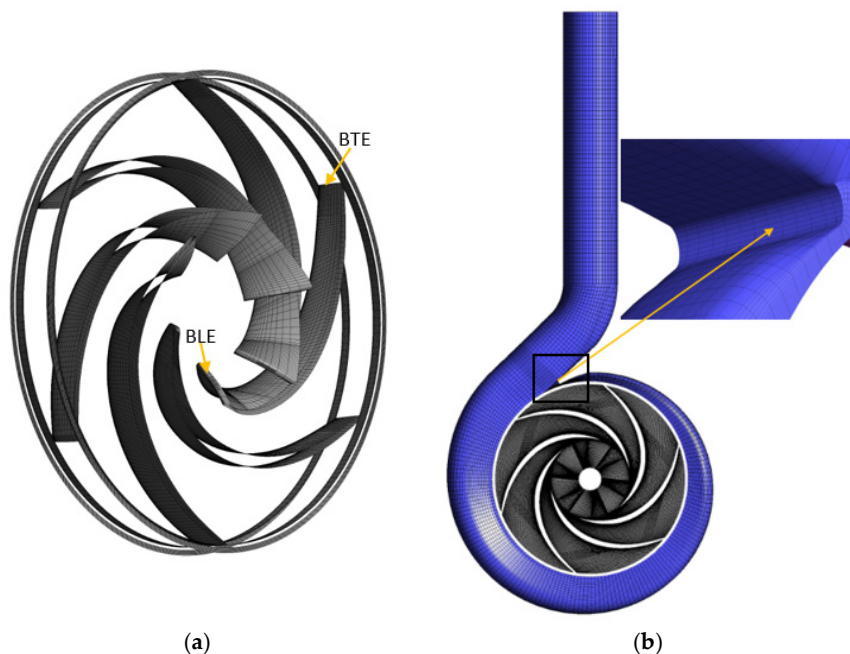


Figure 11. Mesh of (a) impeller blades with (BLE denoting blade leading edge and BTL denoting blade trailing edge) volute with volute tongue enlargement.

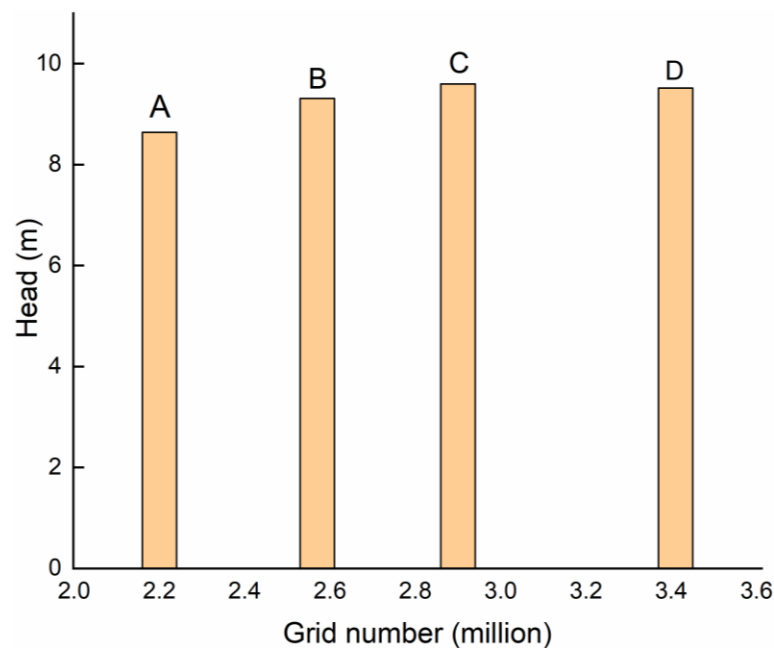


Figure 12. Grid-sensitivity analysis.

In order to predict the pressure head and efficiency at each flow condition, these variables were evaluated by averaging all values at each iteration from the steady numerical simulations. The efficiency of the pump and PAT was evaluated using Equations (58) and (59) respectively:

$$\eta = \frac{\rho g Q H}{T \omega} \quad (58)$$

$$\eta = \frac{T \omega}{\rho g Q H} \quad (59)$$

where T (Nm), is the torque on the shaft, ω (rad/s) is the angular velocity of the impeller.

The head was subsequently evaluated using Equation (60):

$$H = \frac{P_{\text{out}} - P_{\text{in}}}{\rho g} \quad (60)$$

where P (m) denotes the pressure head of the pump and subscript in and out denote the inlet and the outlet of the pump.

4.1.2. Experimental Test of PAT on Pump Mode

The centrifugal pump performance curves are measured in a closed test rig, at National Research Center of Pumps (Jiangsu University) as presented in Figure 13. The geometrical and operational parameters of the PAT are listed in Table 1. The flow rate is measured by LWGY-65 turbine flowmeter with accuracy of 0.2%. The inlet and outlet pressure is tested using static pressure sensor produced by WIKA and both of the accuracy are 0.25%. The torque is measured with SGD-50 torque sensor with a high accuracy of 0.05%. The performance data is acquired with LabView from a NI USB- 6343 data acquisition card. With a 10 times repeated experimental measurement of the performance at design point, the total uncertainty is $\pm 0.56\%$.



Figure 13. The closed test rig of PAT on pump mode.

4.1.3. Validation of PAT Model

In order to justify the validity of our 1-D theoretical model, Figure 14a–c depicts the comparison of the pressure head loss in both CFD and theoretical model of the pump and turbine modes. Different components of the PAT including the volute, impeller and outlet are presented separately. The pressure head loss curves of the CFD and theoretical model show a similar characteristic trend with minimal deviation. As established in Figure 14, the magnitude of the head losses is not the same in both pump and turbine modes. The pressure head is observed to decrease from the part load to the design flow rate region and to increase afterward at the overload region as the flow rate increases. In the volute geometry, the magnitude of the pressure head loss in the pump mode is greater than that of turbine mode as the flow rate increases. However, in turbine mode the magnitude of the pressure head loss that occurs in the impeller and the outlet pipe (inlet pipe in pump mode) geometry is higher than in pump mode. These variations of the pressure head loss exist because the energy transfer from the rotating impeller to the fluid or vice-versa is not achieved in the same way.

Figure 15 shows the numerical simulated results of PAT in pump mode, theoretical predicted model and the experimental results. The results show that the tendency of characteristic curves is accurately predicted by the proposed theoretical model. The experimental, CFD and theoretical model characteristic curves show a similar tendency of a quadratic curve. The efficiency curves increased from the part-load region to the BEP and thereafter decreased towards the overload region. The pressure heads also showed a decreased trend as the flow rate increases. The simulated head and efficiency at the best efficiency point are 9.62 m and 80.2% and it occurred at a flow rate of 27.5 m³/h. The deviations of head and efficiency at BEP are 4.4% and 0.69% respectively with respect to the CFD results, and the discrepancy increases with the increasing flow rate. Therefore, the optimization on performance improvement based on numerical simulations can be reliable.

Figure 16 shows the comparison results of the theoretical model and simulation of PAT efficiency and head in the turbine mode. The error of the theoretical PAT efficiency is less than 2% at the BEP. The simulated efficiency is 75.42% at the best efficiency point (BEP). The error of the theoretical PAT head at the BEP is less than 3% and the simulated head is 9.8 m. The BEP of PAT occurred at a flow rate of 30 m³/h respectively on both theoretical and CFD characteristics curves. The results of the theoretical characteristic curves show that the prediction accuracy meets the simulation standards. Also, it can be established that the efficiency of the curves varies throughout the operating range. Both the CFD and theoretical model characteristic curves show a similar tendency of a quadratic curve. The efficiency of both curves increased from the part-load region to the BEP and thereafter decreased towards the overload region. The predicted flow rate at the BEP under PAT mode by Sharma [23] prediction equation as expressed in Equation (9) is 32.47 m³/h, which is quite close to 30 m³/h of the numerical simulations, with a relative deviation of 7.6%.

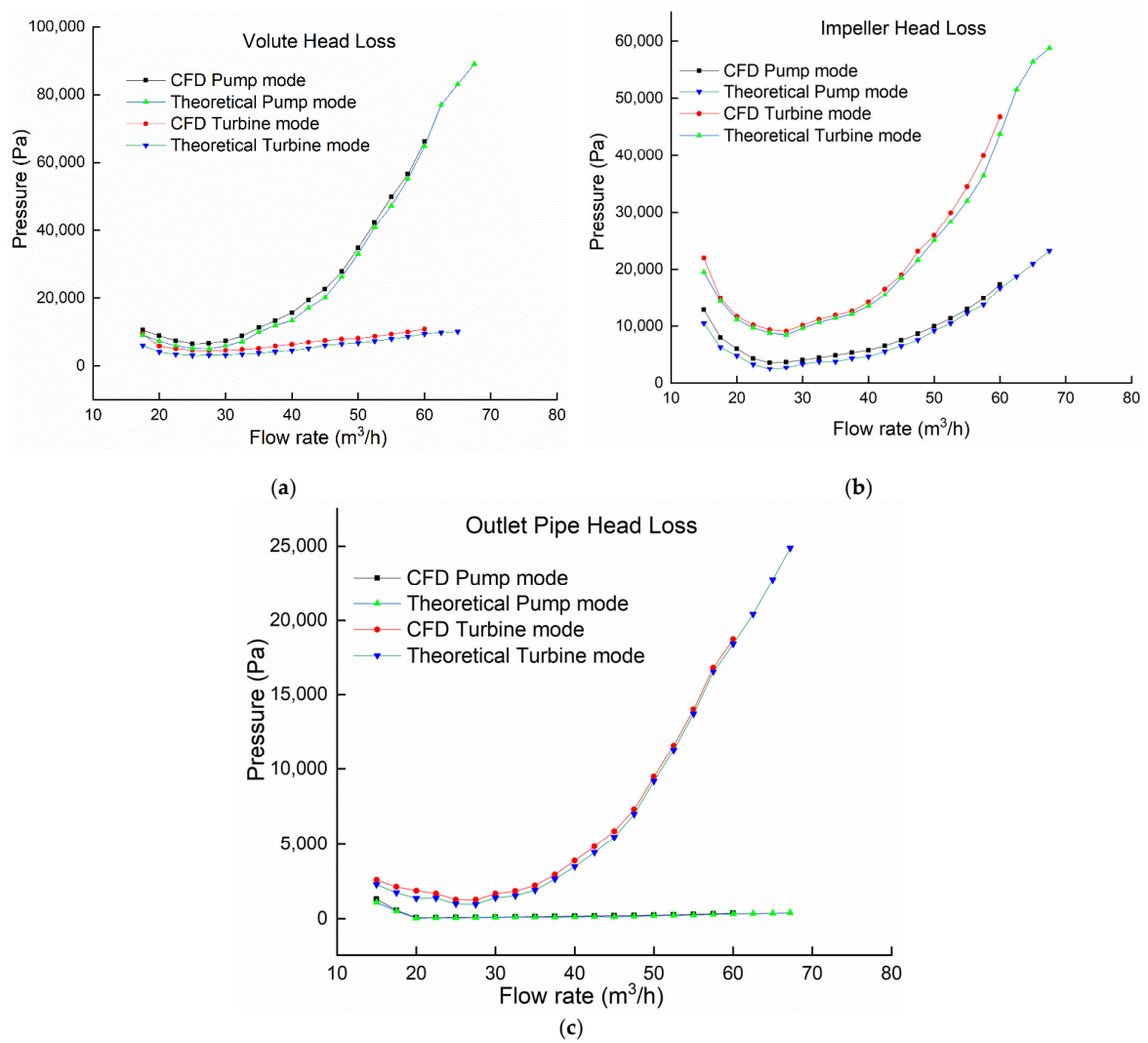


Figure 14. Magnitude of pressure head loss: (a) Volute (b) Impeller (c) Outlet pipe.

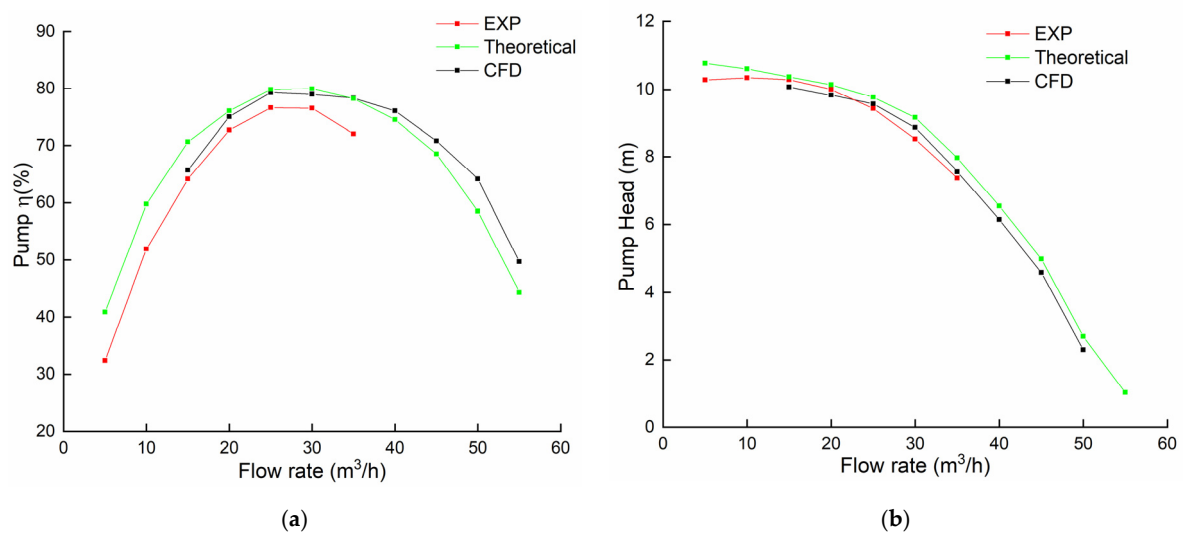


Figure 15. Prediction performance of PAT for (a) pump mode efficiency (b) pump mode head.

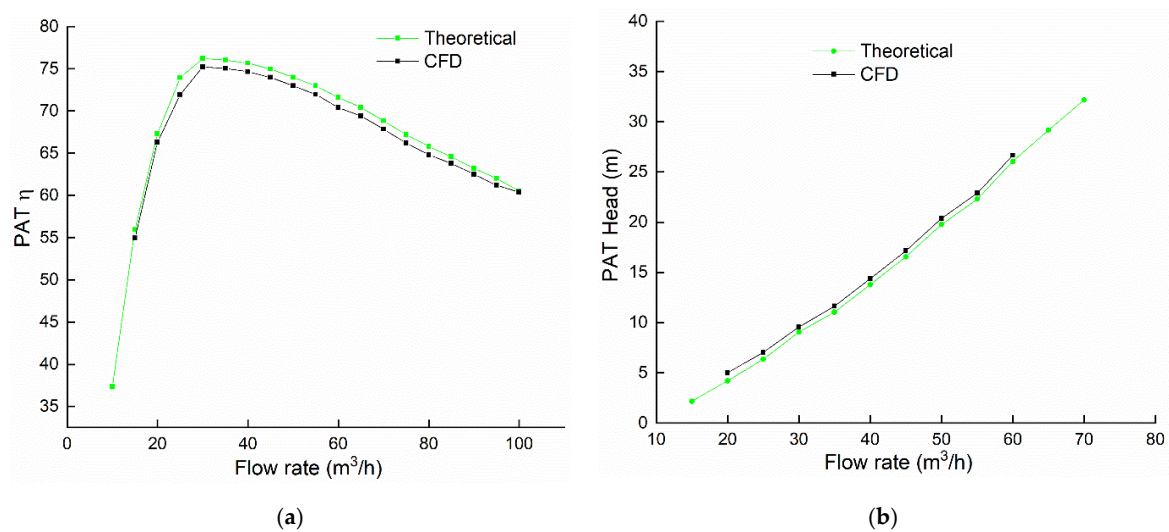


Figure 16. Prediction performance of PAT for (a) turbine mode efficiency (b) turbine mode head.

When the PAT impeller rotate with the fluid, the pressure energy of the fluid is converted into mechanical energy on the impeller shaft. This mechanical energy is expressed as the product of the impeller rotating shaft torque and rotational angular velocity. Equation (61) is a mathematical expression used to calculate the mechanical energy. Figure 17 shows the energy conversion of the impeller to the shaft at different flow rates. It can be observed that as the flow rate increases the output power increases along. Both the CFD and theoretical model characteristic curves shows a similar increasing tendency:

$$P_{\text{out}} = T\omega \quad (61)$$

where T is the torque and ω is the impeller rotation angular velocity.

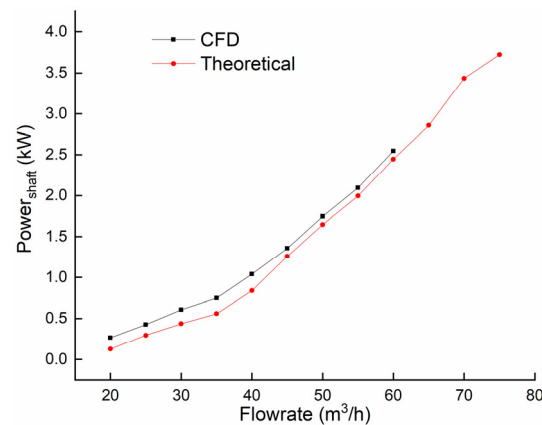


Figure 17. Power generated by the PAT.

4.2. Theoretical Optimization Results

The Pareto-Based Genetic Algorithm was used to obtain an optimization model. The 2D Pareto frontiers from PBGA from the two objective functions are shown in Figure 18. A set of 1000 Pareto optimal combinations was presented in a Pareto solution set which satisfied both objective functions.

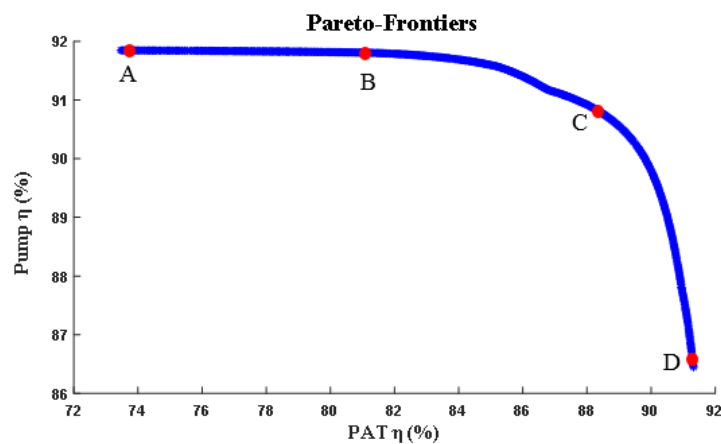


Figure 18. Pareto-frontiers.

The Pareto optimal set is a set of non-dominated solutions with respect to one another. When going from one Pareto solution to another, there is always a certain amount of loss in one target to accomplish any gain in the other. Pareto optimal solution sets are often compared to single solutions because they can be realistic in circumstances of real life. In real pump usage, there is a need to maximize economic benefits. Four points were selected from the Pareto optimal solution set as depicted in Figure 18 with red dots highlighted, to investigate the objectives set for these studies.

The four points selected from the Pareto optimal solution set were compared with the theoretical model in Figures 19 and 20. A new impeller was modeled with the theoretical model in reference to the optimum decision variables in Table 9. The theoretical model efficiencies and the predicted results from the four optimal cases at the design flow rate were compared. Though the head is not an optimization objective, it should not be made poorer. In case A, the pump efficiency increased by 3.9% with 2.43% dropped in efficiency at turbine mode, the pressure head drops by 14.1% in pump mode and 31.5% increase in turbine mode. The efficiency of case B increased by 2.38% in pump mode and dropped by 2% in turbine mode. The pressure head in pump mode drops by 2.5% but the turbine mode witnessed an increase of 47.2%. The case C recorded a negative pressure head of about 5.8% in pump mode with a 70% increase in turbine mode, the efficiencies of both pump and turbine modes recorded an increase of 0.18% and 17% respectively. The case D also recorded a negative pressure head of about 10.6% in pump mode with a 26% increase in turbine mode, the efficiency of the pump drooped by 5.6% and increased by 25.4% in turbine mode. Since all the cases are the optimal solutions to the objective functions, the summarization of the optimized case deviations have been presented in Table 10.

Table 9. Variables for optimal cases.

Case	b_2	β_2	β_1	z	PAT η (%)	Pump η (%)
A	0.010	20.03	21.38	5	72	93.4
B	0.012	20.8	20.10	7	72.2	91.80
C	0.012	25.58	20.08	5	87	90.82
D	0.015	34.80	20.15	4	92	84.48

Table 10. Summarization of the optimized case deviations.

Properties	Case A	Case B	Case C	Case D
Pump η (%)	3.97	2.38	0.18	−5.6
PAT η (%)	−2.43	−2	17	25.4
Pump Head (m)	−14.2	−2.5	−5.8	−10.67
PAT Head (m)	31.5	47.2	70	26

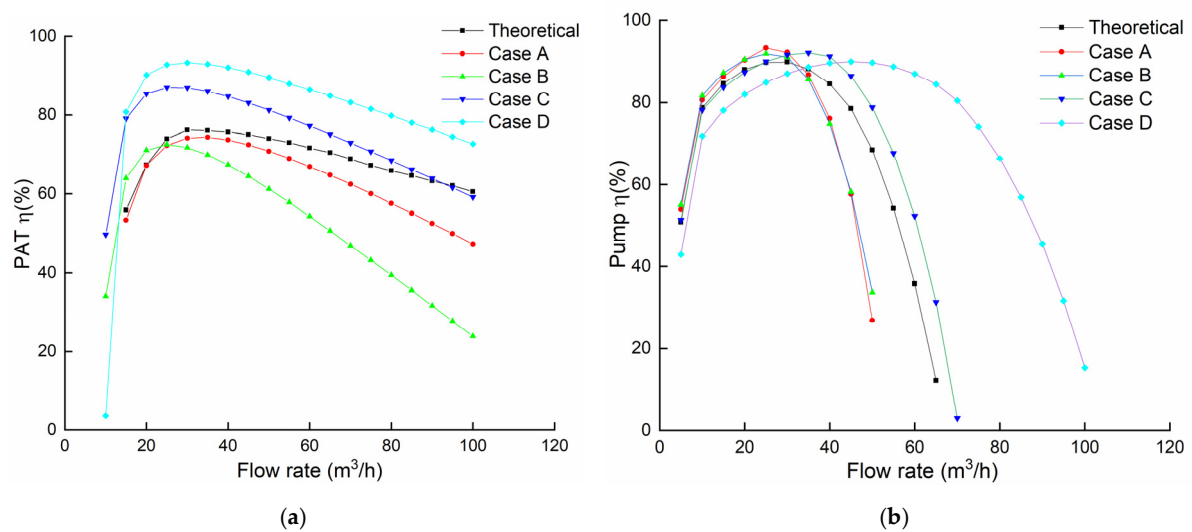


Figure 19. Optimized efficiencies of (a) PAT and (b) pump respectively.

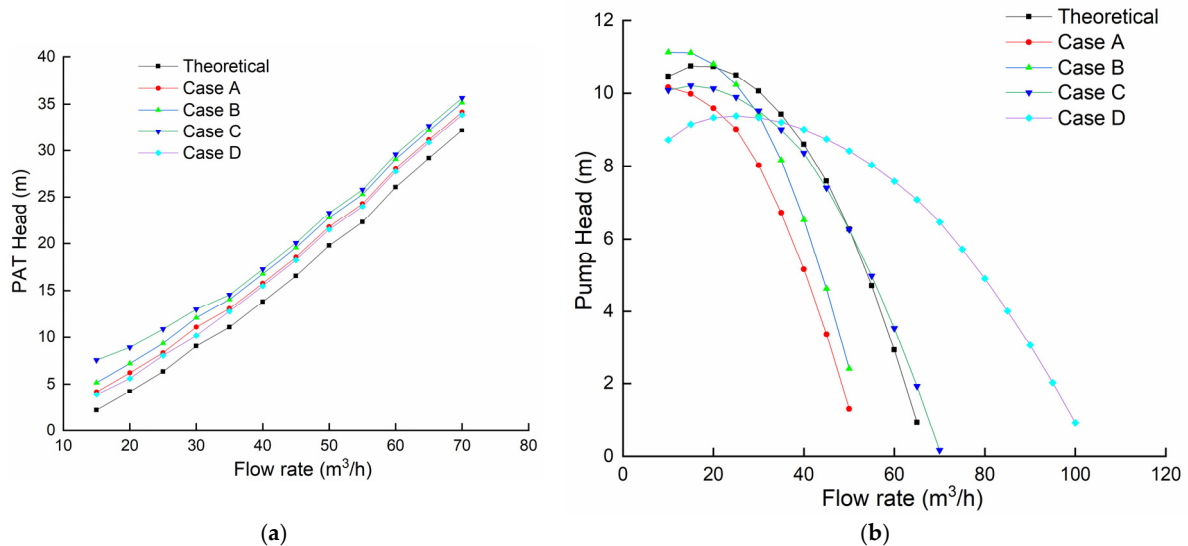


Figure 20. Optimized head of (a) PAT and (b) pump respectively.

Even though case D had a better efficiency performing than cases C and A in turbine mode, in pump mode case A and B efficiencies were slightly better than case D and C at design flow rate. The pressure head should not be made worse off by the optimized parameters, as a result, case C is selected because it generated a pump mode efficiency increase of 0.18% and a head reduction of 5.8% while in turbine mode, the efficiency and head increase by 17% and 70% respectively at the design flow condition. Therefore optimized case C would be best suited for the multi-objective optimization since it increases in efficiencies for both pump and turbine modes with a suitable pressure head.

The numerical simulation and the theoretical model of case C in both pump and PAT modes are presented in Figure 21. In both modes, the results show that the proposed theoretical model accurately predicts the tendency of characteristic curves. The average relative deviations between the theoretical model and numerical simulations is 0.89% in PAT mode and 2.65% in pump mode at the BEP.

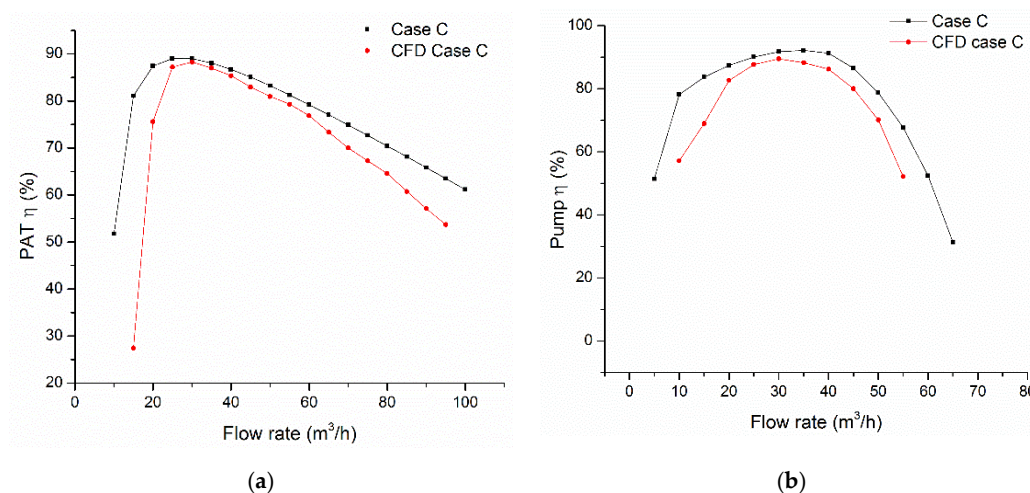


Figure 21. Prediction of energy performance in (a) under PAT mode (b) under pump mode.

5. Conclusions

In this study, a theoretical attempt is made to optimize and predict the performance of a centrifugal pump operating as PAT by modeling and analyzing all the various flow losses in the pump at both pump and turbine operating modes.

It has been established that the proposed theoretical model can predict the general characteristics of the PAT performance well. Based on the theoretical optimization results, the geometry of the impeller is redesigned to suit both pump and PAT mode operations. It was also established that the chosen design variables (b_2 , β_1 , β_2 , and z) have a significant influence on the output parameters based on the orthogonal test. The result shows that the efficiencies of the optimized PAT under both pump and turbine modes have improved by 0.27% and 16.3% respectively at the design condition.

The validation of the theoretical model is mandatory, owing to which a numerical investigation was performed to confirm the proposed theoretical performance curves. It has been proven that the predicted results agree well with simulated results, which authenticates the accuracy and reliability of the proposed theoretical model of the performance prediction, under pump and PAT modes. After the optimization, the average relative deviations between the theoretical model and numerical simulations in both PAT and pump efficiencies are 0.89% and 2.65% respectively at the BEP.

As the hydraulic loss model is subject to limitations, it is advisable to further investigate the parameters experimentally and numerically, as the theoretical optimization has given a fair idea of the effect of the chosen parameters on the hydraulic performance in both pump and PAT mode operations [58–60]. This approach will extensively save time and other resources. For future research work, it is recommended that there should be continuous evaluation of test data with the aid of design variables to further extend the catalogue when designing new impellers and volutes [61,62]. Moreover, the pump volute should be extensively researched to help broaden our knowledge on how it affects the overall performance [63]. The pump volute model should be expanded to cover the pump tongue distance and mismatch between the impeller and the volute flow angle.

Author Contributions: Conceptualization, L.W. and J.Y.; methodology, L.W. and S.N.A.; data curation, S.N.A.; writing—original draft preparation, S.N.A.; writing—review and editing, L.W.; software, D.A.; funding acquisition, J.Y. All authors have read and agreed to the published version of the manuscript.

Funding: This study is financially supported by the China Postdoctoral Science Foundation (Grant No. 2018M632244), Natural Science Foundation of Jiangsu Province (Grant No. BK20180879), High-level Talent Research Foundation of Jiangsu University (Grant No. 18JDG012).

Acknowledgments: The everlasting love and support from the first author's fiancé Lei Wang are gratefully acknowledged, and moreover this work is a gift of proposal to her.

Conflicts of Interest: The authors declare no conflict of interest.

Nomenclature

Symbols

Δh_T	total head loss	(m)
Δh_{inlet}	pipe inlet head loss	(m)
Δh_{outlet}	pipe outlet head loss	(m)
Δh_{inc}	incidence head loss	(m)
Δh_{sfl}	surface frictional head loss	(m)
Δh_{bl}	blade loading head loss	(m)
Δh_{sl}	separation head loss	(m)
Δh_{rec}	recirculation power loss	(W)
Δh_{mix}	wake mixing head loss	(m)
Δh_{df}	disk friction power loss	(W)
Δh_{lk}	leakage power loss	(W)
Δh_{vl}	spiral part incidence head loss	(m)
Δh_{vfl}	spiral friction head loss	(m)
Δh_{vdiff}	diffuser part friction head loss	(m)
Δh_{vsl}	diffuser part separation head loss	(m)
H	head	(m)
D	diameter	(m)
Dj	inlet diameter	(m)
Q	flow rate	(m ³ /h)
η	efficiency	
ρ	density of the liquid	(kg/m ³)
P	power	(W)
n_s	specific speed	
C	conversion factors	
ε	blade thickness coefficient	
ω	angular velocity	(rads ⁻¹)
n	rotational speed	(rpm)
z	blade number	
σ	slip factor	
Δh	head loss	(m)
u	impeller periphery velocity	
w	relative velocity	(ms ⁻¹)
v	absolute velocity	(ms ⁻¹)
α	absolute flow angle	(°)
β	relative angle	(°)
γ	specific weight of fluid	(Nm ⁻³)
λ	friction coefficient	
A	area	(m ²)
T	torque on the shaft	(Nm)

Subscripts

Max	maximum
Min	minimal
1	impeller inlet
2	impeller outlet
3	volute section
4	volute throat section
5	volute discharge section
r	radial
t	turbine
p	pump
θ	tangential direction
in	pump inlet
out	pump outlet

Abbreviations

BEP	best efficiency point
SST	shear stress transport
1D	1-dimensional
3D	3-dimensional
N-S	Navier-Stokes
CFD	computational fluid dynamics
PAT	Pump-as-turbine
W	Watt

References

- Smith, K.A.; Gupta, J.N.; Smith-Miles, K. Neural networks in business: Techniques and applications for the operations researcher. *Comput. Oper. Res.* **2000**, *27*, 1023–1044. [\[CrossRef\]](#)
- Tamm, A. Analysis of a standard pump in reverse operation using CFD. In Proceedings of the 20th IAHR Symposium, Charlotte, NC, USA, 6–9 August 2000.
- Derakhshan, S.; Nourbakhsh, A. Theoretical, numerical and experimental investigation of centrifugal pumps in reverse operation. *Exp. Therm. Fluid Sci.* **2008**, *32*, 1620–1627. [\[CrossRef\]](#)
- Asomani, S.N.; Yuan, J.; Wang, L.; Appiah, D.; Zhang, F. Geometrical effects on performance and inner flow characteristics of a pump-as-turbine: A review. *Adv. Mech. Eng.* **2020**, *12*, 1687814020912149. [\[CrossRef\]](#)
- Carravetta, A.; Del Giudice, G.; Fecarotta, O.; Ramos, H. PAT Design Strategy for Energy Recovery in Water Distribution Networks by Electrical Regulation. *Energies* **2013**, *6*, 411–424. [\[CrossRef\]](#)
- Carravetta, A.; Del Giudice, G.; Fecarotta, O.; Ramos, H. Pump as Turbine (PAT) Design in Water Distribution Network by System Effectiveness. *Water* **2013**, *5*, 1211–1225. [\[CrossRef\]](#)
- Carravetta, A.; Del Giudice, G.; Fecarotta, O.; Ramos, H.M. Energy Production in Water Distribution Networks: A PAT Design Strategy. *Water Resour. Manag.* **2012**, *26*, 3947–3959. [\[CrossRef\]](#)
- Strategen Consulting, L. *DOE Global Energy Storage Database*; Sandia National Laboratories: Livermore, CA, USA, 2016.
- Morabito, A.; Hendrick, P. Pump as turbine applied to micro energy storage and smart water grids: A case study. *Appl. Energy* **2019**, *241*, 567–579. [\[CrossRef\]](#)
- Gimeno-Gutiérrez, M.; Arántegui, R.L. Assessment of the European potential for pumped hydropower energy storage based on two existing reservoirs. *Renew. Energy* **2015**, *75*, 856–868. [\[CrossRef\]](#)
- Polák, M. The Influence of Changing Hydropower Potential on Performance Parameters of Pumps in Turbine Mode. *Energies* **2019**, *12*, 2103. [\[CrossRef\]](#)
- Rossi, M.; Nigro, A.; Renzi, M. Experimental and numerical assessment of a methodology for performance prediction of Pumps-as-Turbines (PaTs) operating in off-design conditions. *Appl. Energy* **2019**, *248*, 555–566. [\[CrossRef\]](#)
- Yang, S.-S.; Kong, F.-Y.; Chen, H.; Su, X.-H. Effects of Blade Wrap Angle Influencing a Pump as Turbine. *J. Fluids Eng.* **2012**, *134*, 061102. [\[CrossRef\]](#)
- Yang, S.-S.; Derakhshan, S.; Kong, F.-Y. Theoretical, numerical and experimental prediction of pump as turbine performance. *Renew. Energy* **2012**, *48*, 507–513. [\[CrossRef\]](#)
- Capurso, T.; Stefanizzi, M.; Pascazio, G.; Ranaldo, S.; Camporeale, S.M.; Fortunato, B.; Torresi, M. Slip Factor Correction in 1-D Performance Prediction Model for PaTs. *Water* **2019**, *11*, 565. [\[CrossRef\]](#)
- Capurso, T.; Stefanizzi, M.; Pascazio, G.; Camporeale, S.M.; Torresi, M. Dependency of the slip phenomenon on the inertial forces inside radial runners. In Proceedings of the Second International Conference on Material Science, Smart Structures and Applications: ICMSS-2019, Erode, India, 21–22 November 2019; AIP Publishing: New York, NY, USA, 2019; Volume 2191, p. 020034.
- Williams, A. Prelims-Pumps as Turbines. In *Pumps as Turbines: A Users Guide*; Practical Action Publishing: Warwickshire, UK, 1995; pp. i–x.
- Singh, P.; Nestmann, F. An optimization routine on a prediction and selection model for the turbine operation of centrifugal pumps. *Exp. Therm. Fluid Sci.* **2010**, *34*, 152–164. [\[CrossRef\]](#)
- Ramos, H.M.; Borgå, Å. Pumps as turbines: An unconventional solution to energy production. *Urban Water* **1999**, *1*, 261–263. [\[CrossRef\]](#)

20. Wang, X.H.; Jun, H.Y.; Feng, X.S.; Ren, H.Z. Theoretical and Numerical Study of Performance Prediction of Centrifugal Pumps as Turbines. In *Applied Mechanics and Materials*; Trans Tech Publ.: Stafa-Zurich, Switzerland, 2014. Available online: <https://www.scientific.net/AMM.444-445.579> (accessed on 1 June 2020).
21. Derakhshan, S.; Mohammadi, B.; Nourbakhsh, A. Efficiency Improvement of Centrifugal Reverse Pumps. *J. Fluids Eng.* **2009**, *131*, 021103. [[CrossRef](#)]
22. Li, Y.G.; Ghafir, M.F.A.; Wang, L.; Singh, R.; Huang, K.; Feng, X. Nonlinear Multiple Points Gas Turbine Off-Design Performance Adaptation Using a Genetic Algorithm. *J. Eng. Gas Turbines Power* **2011**, *133*, 071701. [[CrossRef](#)]
23. Sharma, K.J.K.E.C. *Small Hydroelectric Project-Use of Centrifugal Pumps as Turbines*; Kirloskar Electric. Co.: Bangalore, India, 1985.
24. Alatorre-Frenk, C. *Cost Minimisation in Micro-Hydro Systems Using Pumps-as-Turbines*; University of Warwick: Coventry, UK, 1994.
25. Stepanoff, A.J.J.T. *Centrifugal and Axial Flow Pumps: Theory, Design, and Application*; John Wiley & Sons: New York, NY, USA, 1957.
26. Williams, A.A. The Turbine Performance of Centrifugal Pumps: A Comparison of Prediction Methods. *Proc. Inst. Mech. Eng. Part A J. Power Energy* **1994**, *208*, 59–66. [[CrossRef](#)]
27. Nelik, L. *Centrifugal & Rotary Pumps: Fundamentals with Applications*; CRC Press: Boca Raton, FL, USA, 1999.
28. Krivchenko, G.J.T. *Hydraulic Machines Turbines and Pumps*; CRC-Press: Florence, KY, USA, 1994; pp. 368–369.
29. McClaskey, B.; Ja, L. Can you justify hydraulic turbines. *Hydrocarb. Process.* **1976**, *55*, 163–169.
30. Yang, S.; Kong, F.; Chen, H.; Su, X. Effects of blade inlet angle on performance of pump as turbine. *J. Cent. South Univ.* **2013**, *1*.
31. Zhang, J.; Appiah, D.; Zhang, F.; Yuan, S.; Gu, Y.; Asomani, S.N. Experimental and numerical investigations on pressure pulsation in a pump mode operation of a pump as turbine. *Energy Sci. Eng.* **2019**, *7*, 1264–1279. [[CrossRef](#)]
32. Wang, L.; Tan, A.; Cholette, M.; Gu, Y. Comparison of the effectiveness of analytical wake models for wind farm with constant and variable hub heights. *Energy Convers. Manag.* **2016**, *124*, 189–202. [[CrossRef](#)]
33. Stodola, A. *Steam and Gas Turbines: With a Supplement on the Prospects of the Thermal Prime Mover*; McGraw-Hill: New York, NY, USA, 1927; Volume 2.
34. Derakhshan, S.; Nourbakhsh, A. Experimental study of characteristic curves of centrifugal pumps working as turbines in different specific speeds. *Exp. Therm. Fluid Sci.* **2008**, *32*, 800–807. [[CrossRef](#)]
35. Conrad, O.; Raif, K.; Wessels, M. The Calculation of performance maps for centrifugal compressors with vane-island diffusers. In *Performance Prediction of Centrifugal Pumps and Compressors*; NASA Astrophysics Data System: Cambridge, MA, USA, 1979. Available online: <https://ui.adsabs.harvard.edu/abs/1979ppcp.proc..135C/abstract> (accessed on 1 June 2020).
36. Gülich, J.F. Pump Hydraulics and Physical Concepts. In *Centrifugal Pumps*; Springer: Berlin/Heidelberg, Germany, 2010; pp. 69–144.
37. Hodge, B.K. Analysis and Design of Energy Systems. 1984. Available online: https://www.researchgate.net/publication/236401810_Analysis_and_Design_of_Energy_Systems (accessed on 1 June 2020).
38. Lieblein, S.; Schwenk, F.C.; Broderick, R.L. *Diffusion Factor for Estimating Losses and Limiting Blade Loadings in Axial-Flow-Compressor Blade Elements*; National Advisory Committee For Aeronautics: Cleveland Oh Lewis Flight: Cleveland, OH, USA, 1953.
39. Coppage, J.; Dallenbach, F. Study of supersonic radial compressors for refrigeration and pressurization systems. *Inf. Process. Lett.* **1956**, *1*, 157–163.
40. Tuzson, J. *Centrifugal Pump Design*; John Wiley & Sons: Hoboken, NJ, USA, 2000.
41. Djebdjan, B.J.M.E.J. Theoretical model to predict the performance of centrifugal pump equipped with splitter blades. *Mansoura Eng. J.* **2009**, *34*, 50–70.
42. Johnston, J.P.; Dean, R.C. Losses in Vaneless Diffusers of Centrifugal Compressors and Pumps: Analysis, Experiment, and Design. *J. Eng. Power* **1966**, *88*, 49–60. [[CrossRef](#)]
43. Thin, K.C.; Khaing, M.M.; Aye, K.M. Design and performance analysis of centrifugal pump. *World Acad. Sci. Eng. Technol.* **2008**, *46*, 422–429.
44. Omar, A.K.; Khaldi, A.; Ladouani, A. Prediction of centrifugal pump performance using energy loss analysis. *Aust. J. Mech. Eng.* **2016**, *15*, 210–221. [[CrossRef](#)]

45. El-Naggar, M.A. A One-Dimensional Flow Analysis for the Prediction of Centrifugal Pump Performance Characteristics. *Int. J. Rotating Mach.* **2013**, *2013*, 1–19. [[CrossRef](#)]
46. Tan, L. Modeling and experiment of the hydraulic losses of centrifugal pump with inlet guide vanes. *Shuili Fadian Xuebao/J. Hydroelectr. Eng.* **2011**, *30*, 191–196.
47. Huang, S.; Qiu, G.; Su, X.; Chen, J.; Zou, W. Performance prediction of a centrifugal pump as turbine using rotor-volute matching principle. *Renew. Energy* **2017**, *108*, 64–71. [[CrossRef](#)]
48. Wyss, G.; Jorgensen, K. *A Users Guide to LHS: Sandias Latin Hypercube Sampling Software*; Sandia National Labs.: Albuquerque, NM, USA, 1998. [[CrossRef](#)]
49. Jin, R.; Chen, W.; Simpson, T. Comparative studies of metamodeling techniques under multiple modelling criteria. *Struct. Multidiscip. Optim.* **2001**, *23*, 1–13. [[CrossRef](#)]
50. Pei, J.; Yin, T.; Yuan, S.; Wang, W.; Wang, J. Cavitation optimization for a centrifugal pump impeller by using orthogonal design of experiment. *Chin. J. Mech. Eng.* **2017**, *30*, 103–109. [[CrossRef](#)]
51. Zhou, L.; Shi, W.; Wu, S. Performance Optimization in a Centrifugal Pump Impeller by Orthogonal Experiment and Numerical Simulation. *Adv. Mech. Eng.* **2013**, *5*, 385809. [[CrossRef](#)]
52. Gen, M.; Cheng, R. *Genetic Algorithms and Engineering Optimization*; John Wiley & Sons: Hoboken, NJ, USA, 2000; Volume 7.
53. Matlab. *The Language of Technical Computing-Release 14*; The MathWorks Inc.: Natick, MA, USA, 2004.
54. Afzal, A.; Kim, K.-Y. Multi-Objective Optimization of a Passive Micromixer Based on Periodic Variation of Velocity Profile. *Chem. Eng. Commun.* **2014**, *202*, 322–331. [[CrossRef](#)]
55. Kulkarni, K.; Afzal, A.; Kim, K.-Y. Multi-objective optimization of solar air heater with obstacles on absorber plate. *Sol. Energy* **2015**, *114*, 364–377. [[CrossRef](#)]
56. Shim, H.-S.; Kim, K.-Y.; Choi, Y.-S. Three-Objective Optimization of a Centrifugal Pump to Reduce Flow Recirculation and Cavitation. *J. Fluids Eng.* **2018**, *140*, 091202. [[CrossRef](#)]
57. Asomani, S.N.; Yuan, J.P.; Wang, L.Y.; Appiah, D. The Impact of Surrogate Models on the Multi-Objective Optimization of Pump-As-Turbine (PAT). *Energies* **2020**, 1–30.
58. Jiang, X.P.; Liu, S.H.; Wang, Y. Effect of outlet back pressure on performance of twin-screw pump as turbine. *J. Drain. Irrig. Mach. Eng.* **2017**, *35*, 1042–1047.
59. Bai, Y.X.; Liu, Y.Y.; Kong, F.Y. Influence of impeller diameter on mixed flow pump as turbine. *J. Drain. Irrig. Mach. Eng.* **2019**, *37*, 284–288.
60. Luo, B.; Wang, C.L.; Xia, Y. Numerical simulation of flow-induced vibration of double-suction centrifugal pump as turbine. *J. Drain. Irrig. Mach. Eng.* **2019**, *37*, 313–318.
61. Yang, S.S.; Shao, K.; Dai, T. Influence of blade wrap angle on characteristics of mixed flow pump as turbine. *J. Drain. Irrig. Mach. Eng.* **2019**, *37*, 475–479.
62. Liu, Y.Y.; Yang, S.S.; Kong, F.Y. Numerical simulation of hydraulic turbines with forward-curved blades. *J. Drain. Irrig. Mach. Eng.* **2018**, *36*, 21–27.
63. Yang, S.S.; Dai, T.; Chen, Z. Influence of volute tilted outlet on performance of mixed-flow pump as turbine. *J. Drain. Irrig. Mach. Eng.* **2020**, *38*, 451–456.

